# Crystallographic Analysis of Hydrogen Embrittlement Behavior in Aluminum Alloy Using Diffraction Contrast Tomography

Hirayama, Kyosuke
Department of Materials Science and Engineering, Kyoto University

Toda, Hiroyuki
Department of Mechanical Engineering, Faculty of Engineering, Kyushu University

Suzuki, Takafumi
Department of Mechanical Engineering, Faculty of Engineering, Kyushu University

Uesugi, Masayuki
Research & Utilization Division, Japan Synchrotron Radiation Research Institute

他

# Crystallographic Analysis of Hydrogen Embrittlement Behavior in Aluminum Alloy Using Diffraction Contrast Tomography

Kyosuke Hirayama[1], Hiroyuki Toda[2], Takafumi Suzuki[2,*], Masayuki Uesugi[3], Akihisa Takeuchi[3] and Wolfgang Ludwig[4]

[1]*Department of Materials Science and Engineering, Kyoto University, Kyoto 606-8501, Japan*
[2]*Department of Mechanical Engineering, Faculty of Engineering, Kyushu University, Fukuoka 819-0395, Japan*
[3]*Research & Utilization Division, Japan Synchrotron Radiation Research Institute, Hyogo 679-5198, Japan*
[4]*European Synchrotron Radiation Facility, BP220, 38043 Grenoble, France*

Crystallographic assessment of the hydrogen embrittlement behavior of Al–Zn–Mg alloy was performed by means of a technique combining fracture trajectory analysis and synchrotron X-ray diffraction contrast tomography. The 3D microstructure reconstructed using diffraction contrast tomography contained 119 grains. Fracture surfaces revealing intergranular fracture, ductile fracture, and quasi-cleavage fracture were observed in the alloy. While the intergranular crack initiated at a grain boundary with high grain boundary energy and a high angle between the grain boundary plane and loading direction, the crack propagation itself was not observed to be sensitive to these two parameters. The quasi-cleavage fracture surfaces were not characterized by any specific crystal orientation because of variation in the free surface segregation energy of hydrogen uniforms without depending on surface orientation.   [doi:10.2320/matertrans.MT-L2021020]

## 1.  Introduction

The presence of hydrogen can change the morphology of the fracture surface of high-strength aluminum alloys from ductile to brittle fracture, as observed in intergranular or quasi-cleavage fracture (hereinafter QCF).[1–5] Christodoulou and Flower reported that such embrittlement is caused primarily by hydrogen trapped at the grain boundaries, which promotes intergranular fracture in Al–6Zn–3Mg alloy.[1] Takano noted that QCF surface was observed on the hydrogen embrittled fracture surfaces in 7075 aluminum alloy, and may occur as a result of an interaction between hydrogen and dislocations.[3] Bond *et al.* observed dense dislocation tangles in front of the crack tip, and reported that hydrogen enhanced the dislocation mobility.[4] Bhuiyan *et al.* observed the influence of hydrogen on the fracture behavior of high strength 7xxx aluminum alloys using synchrotron X-ray microtomography,[5] and observed that the QCF surface fraction area increased with increasing crack tip hydrogen concentration. It may be inferred that QCF occurs along specific crystal planes related to dislocation slip systems of the material. Hydrogen-related QCF in bcc iron single crystals and martensitic and ferritic steels occurs along {011} planes.[6–8] However, the crystal orientation of QCF surface in aluminum alloy is unclear, owing to distortion in the crystal lattice just below the QCF accompanied by plastic deformation.

Recently, using fracture trajectory analysis with X-ray microtomography, Toda *et al.* revealed that the growth of micropores dominates ductile fracture in aluminum alloy.[9] Fracture surfaces are tracked in reverse order, from their final state towards their initial state, making it possible to accurately determine the location of the initiation sites in large strain regions. X-ray diffraction contrast tomography (hereinafter DCT), on the other hand, is a variant of the 3DXRD technique that enables reconstruction of 3D grain maps (grain shape and orientation) in polycrystalline materials.[10] The aim of the present study was to crystallographically assess the hydrogen embrittlement behavior in aluminum alloy, by combining fracture trajectory analysis with X-ray microtomography and diffraction contrast tomography to determine the crystal orientation of QCF surfaces.

## 2.  Experimental Procedure

The material used in the study was Al–Zn–Mg alloy with the following composition (mass%): 10.12 Zn, 1.200 Mg, 0.018 Ti, 0.016 Cu, 0.005 Si, 0.001 Cr. The alloy was homogenized at 773 K for 7.2 ks, and then hot rolled (50% reduction) at 723 K. Subsequently, it was solution treated at 773 K for 0.6 ks. After heat treatment, a two-step aging treatment was applied, at 393 K for 144 ks and 453 K for 25.2 ks. The samples had an equiaxed grain structure with approximately 100 μm average grain size, and were cut by electronic discharge machining (hereinafter EDM) into I-bar shapes as shown in Fig. 1, in order to fit into a tensile rig. The cross-sectional area and gauge length of the specimens were $600 \times 600\,\mu m$ and 700 μm, respectively. It is reported that hydrogen can be charged in the material by preparing the
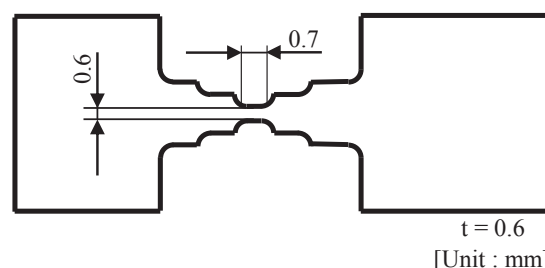


Fig. 1   Specimen geometry for *in-situ* tensile test performed at SPring-8.
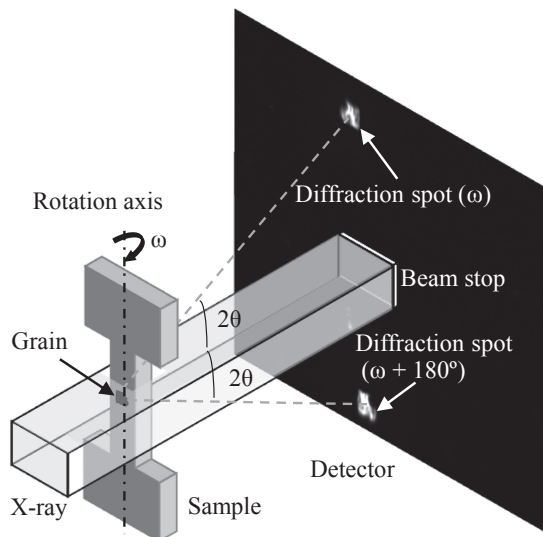
*Graduate Student, Kyushu University

Fig. 2 Schematic representation of DCT experiment setup.



Fig. 3 Stress–strain curves during the *in-situ* tensile testing. Black and white circles show microtomography experiment and DCT experiment, respectively.

specimen using EDM in water,[5] and the total hydrogen content of specimens cut by EDM is 130 times higher than that of raw specimens before cut.

The X-ray microtomography and DCT experiments were carried out using the X-ray imaging beamline, BL20XU, of SPring-8. Figure 2 is a schematic representation of the setup used in this combined experiment. Monochromatic X-ray beams of 20 keV and 30 keV photon energy, generated by liquid nitrogen cooled double Si (111) monochromator, were used for the X-ray microtomography and DCT experiments, respectively. In the X-ray microtomography, the image detector which consisted of a 2048 × 2048-element digital CMOS camera, was placed 20 mm behind the specimen. In total, 1800 radiographs (180°) were obtained around the loading axis in 0.1° increments. The DCT experiment image detector consisted of a 2048 × 2048-element digital CMOS camera placed 8 mm behind the specimen to intercept the diffraction spots from the {111}, {200}, and {220} lattice planes of this aluminum alloy with fcc lattice structure. The effective pixel size of these detectors was 0.5 and 3.1 μm, respectively. For the DCT experiment, the direct X-ray beam was cut off using a center beam stop in front of the detector (Fig. 2), and the sample was rotated through 360° in 0.1° increments. The X-ray microtomography and DCT experiments were conducted as shown in the stress-strain curves in Fig. 3. The first tomographic scan and DCT experiment were performed without loading, and the subsequent five tomographic scans were carried out with loading. The grey value in the X-ray microtomography images was calibrated such that the linear absorption coefficients of 0–40 cm$^{-1}$ fell within an 8-bit grey-scale range between 0 and 255. The volume of each micropore and particle at sub-voxel accuracy is estimated by computing pentagonal faceted iso-intensity surfaces from the volumetric data set, using the Marching Cubes algorithm.[11] Only micropores and particles over 27 voxels in volume were counted as microstructural features in the X-ray microtomography images, in order to reduce inaccuracies originating from image noise.

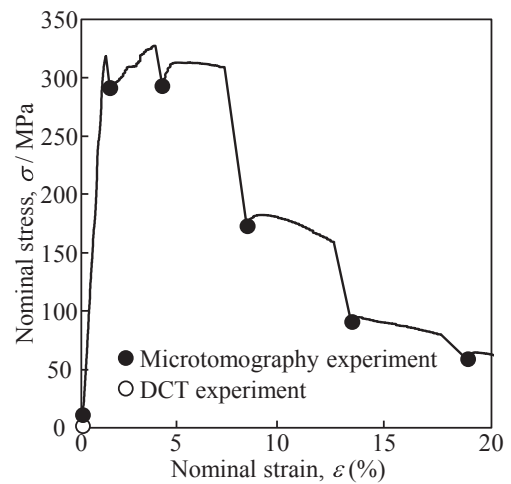To identify the orientation of quasi-cleavage fracture surface in the initial unloaded state, we performed fracture trajectory analysis of a series of X-ray microtomography images.[9] The cracks were tracked in reverse order from the final image of the propagated crack towards the initial state. To predict the invisible trajectory of each crack location in the initial state, the underlying local displacement field was calculated using scattered data interpolation. Radial basis functions were used to calculate interpolants for the physical displacements of all the particles and voids in the sample. The DCT software developed at ESRF was used to analyze the diffraction images, and the diffraction spots were used to reconstruct the grains.[10] The resulting microstructure contained 119 grains.

## 3. Results and Discussion

Figure 4 shows a SEM image of the fracture surface in the Al–Zn–Mg alloy investigated in this synchrotron experiment. The image shows intergranular fracture (hereinafter IGF),
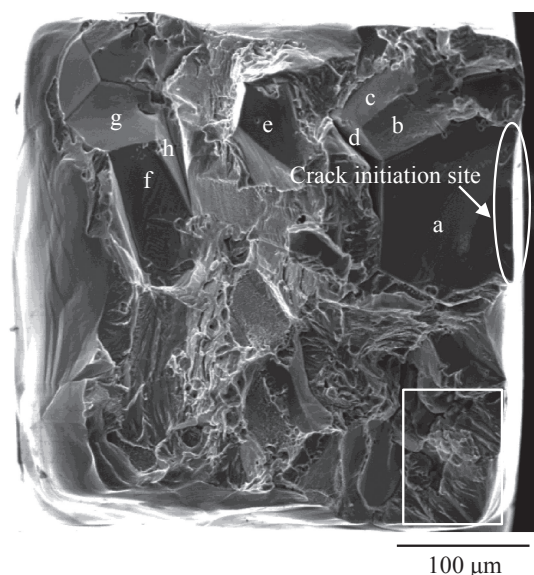


Fig. 4 SEM image of fracture surface in Al–Zn–Mg alloy. Quasi-cleavage surface is highlighted by the white frame.

ductile fracture (hereinafter DF), and QCF surfaces. The respective area fractions of the IGF, DF, and QCF surfaces are approximately 60%, 35%, and 5%. The IGF and QCF surfaces are observable near the specimen surface, while DF surface is found in the center of the specimen. Takano and Bhuiyan have reported that the fracture surface in hydrogen-charged high-strength aluminum alloy changes from DF to IGF and QCF surface depending on the hydrogen concentration.[4,5] The QCF surface, highlighted by the white frame in Fig. 4, consists of multiple smooth and flat regions (see Fig. 7 for a magnified view of this area). The eight IGF surfaces named from a to h in Fig. 4 were tracked towards the initial state from the fracture surface. The IGF surface named a originated from the sample surface as shown by the white dashed circle area in Fig. 4, while the others originated by crack propagation. Figure 5 shows a 3D grain image in the undeformed state, reconstructed from the DCT scan and color-coded (in Fig. 5(a)) according to the inverse pole figure color key shown in the inset. Figure 5(b) shows the predicted IGF surface (crack initiation site) in the gray-scale representation of the grain volume. The average grain size and number of grains in the sample are 71 μm and 119, respectively.

Most of the grain boundaries in the present sample are high-angle random boundaries. A grain boundary energy model for low misorientation angles between adjacent grains ($\theta < 15°$) was proposed by Read and Shockley;[12] however, the model is not useful for the estimation of the grain boundary energy of high-angle grain boundaries because, in this latter case, the dislocation cores begin to overlap and it is impossible to clearly distinguish between a dislocation strain field and a core region in the case of larger misorientation angles ($\theta > 15°$). Thus, in order to calculate the grain boundary energy of high-angle grain boundaries, Wolf extended the Read-Shockley equation to include large misorientation angles:[13]

$$\gamma(\theta) = \gamma_{max} \sin(\theta)[1 - A \ln(\sin(\theta))], \quad (1)$$

where $\gamma(\theta)$ is the grain boundary energy, $\theta$ is the misorientation angle, and $A$ is a constant. $\gamma_{max}$ may be expressed as:

$$\gamma_{max} = Gb/4\pi(1 - \upsilon), \quad (2)$$

where $G$ is the elastic (rigidity) modulus, $b$ is the Burgers vector, and $\upsilon$ is the Poisson coefficient. Figure 6 shows the grain boundary energy and the angle between the grain boundary plane and the loading direction of cracked grain boundaries and grain boundaries connected to the sample surface. The white circle marks the grain boundary where the initial crack occurred, the black circles mark grain boundaries along which the crack propagated, and the gray circles mark uncracked grain boundaries. The crack initiates at a grain boundary with high grain boundary energy and a high angle between the grain boundary plane and loading direction, but its propagation shows no clear dependence on the grain boundary energy and the angle of the grain boundary plane and the loading axis. In polycrystalline material, the quadruple junction point of four grains occasionally exists other than the grain boundary and the triple junction line of three grains. The crack propagation path is limited to a
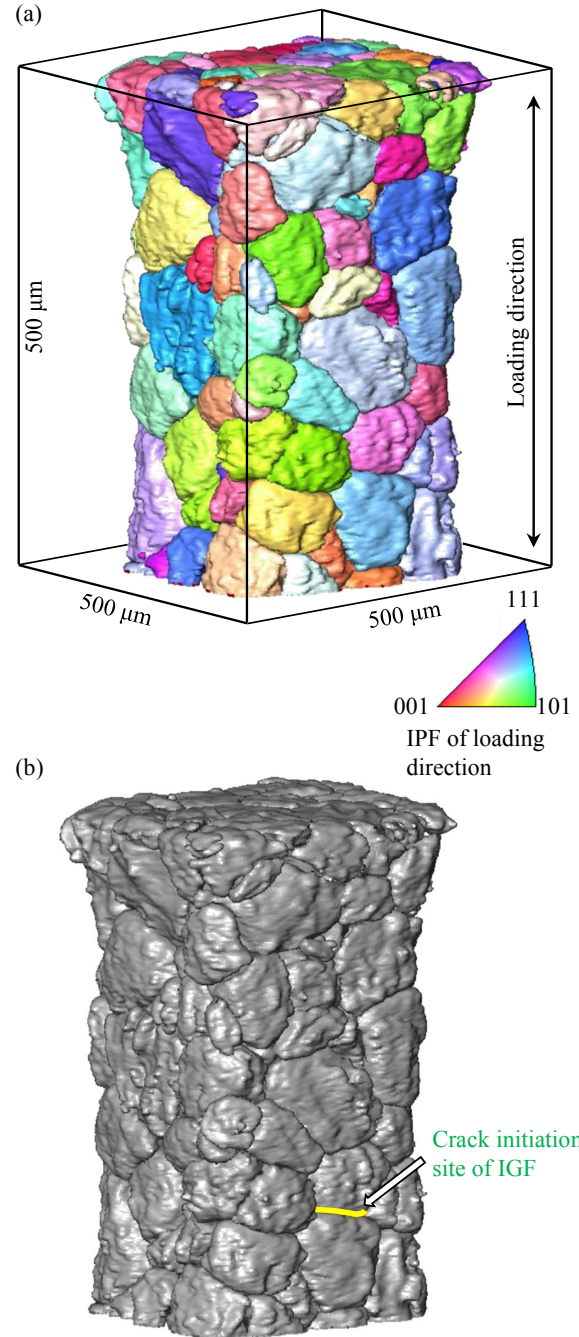


Fig. 5   (a) 3D DCT reconstruction of grains in Al–Zn–Mg alloy. Colors according to IPF key shown in the inset. (b) 3D reconstruction of grains with predicted crack initiation site overlayed in yellow.

maximum of seven paths consisting of six grain boundaries and grain interior, when the crack tip reaches the quadruple junction point. It is considered that the crack propagation is not influenced by the grain boundary energy and the angle of the grain boundary plane and the loading axis. In addition, this lack of correlation indicate that other factors, which are residual stress, grain boundary crystallography, grain boundary segregation, strain incompatibility not considered here, govern the propagation behavior of the cracks.

Figure 7(a) shows a SEM micrograph of QCF surface together with the corresponding region of interest in the combined (DCT + microtomography) dataset (highlighted). This region is fairly close to the surface, and it has been
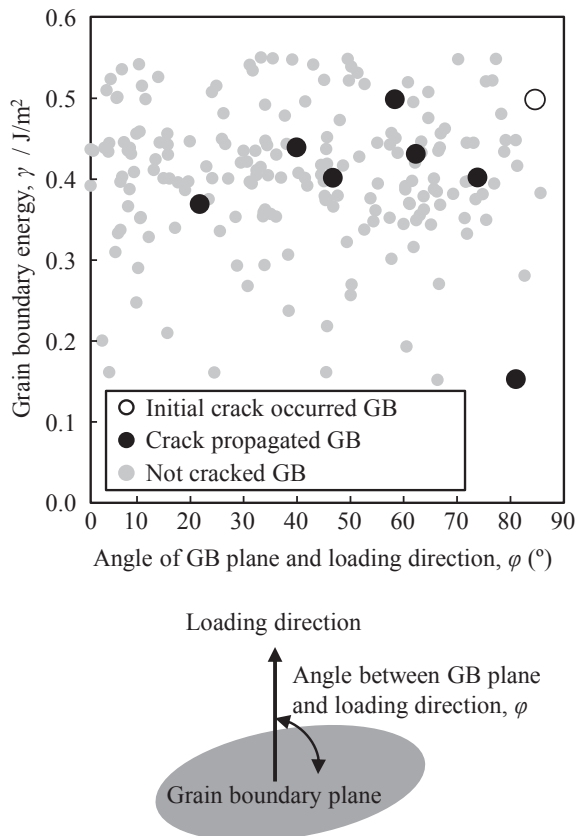
Fig. 6 The relationship of grain boundary energy and angle between grain boundary plane and loading direction of cracked grain boundaries and grain boundaries on the sample surface. The white circle corresponds to the crack initiation site, black ones to grain boundaries along which the crack propagated, gray ones represent the rest of the grain boundary population.
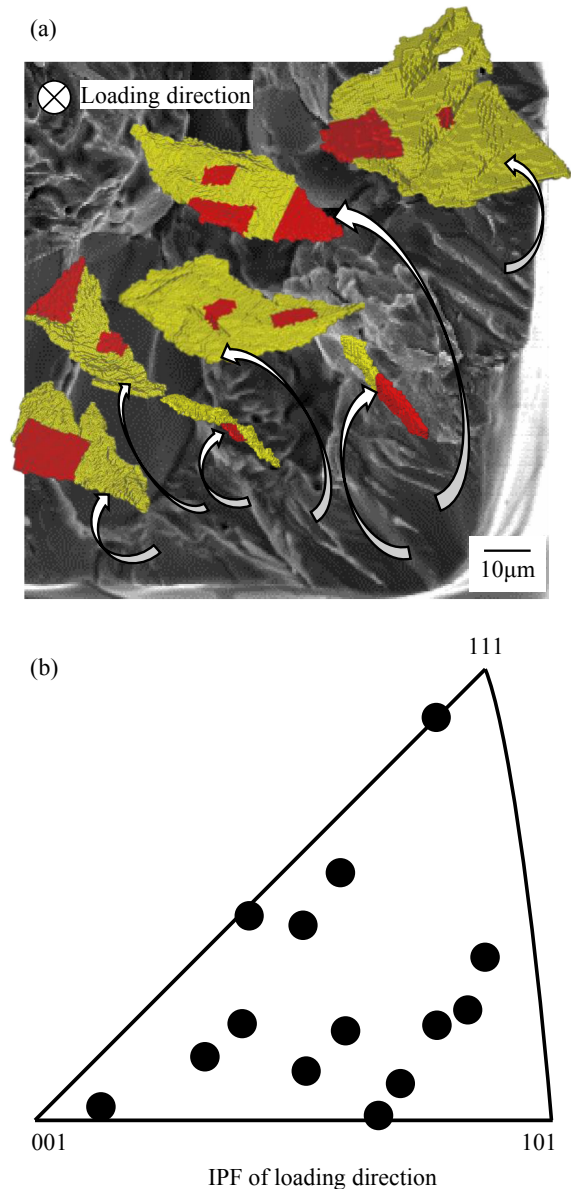


Fig. 7 (a) SEM image and 3-D image of quasi-cleavage fracture surface in Al–Zn–Mg alloy. (b) Inverse pole figure plot of the local crystallographic fracture surface orientations of the red regions in Fig. 5(a).

confirmed that a crack was initiated during the *in-situ* tensile test. It is therefore apparent that this region has not been significantly affected by plastic deformation during the crack propagation, and is suitable for analyzing the appearance and characteristics of QCF. Figure 7(a) is a magnified view of the QCF surface, highlighted by the white frame in Fig. 4. The QCF surface consisted of seven smooth and flat regions across the grain boundary. The seven yellow regions are quasi-cleavage facets are reconstructed into 3D images and extracted from fracture surface. However, as they are not completely flat, but rather slightly curved within the spatial resolution of the X-ray microtomography, flatter regions (here highlighted in red) were extracted from the yellow regions in order to accurately determine the crystallographic orientations of QCF surfaces, for subsequent analysis of the respective crystallographic orientations of the 14 regions along the loading axis shown in Fig. 7(b). It is not observed (111) plane, which is the slip or cleavage plane in FCC metal. The latter cleavage plane has been reported by Defilippi in the case of high manganese FCC steel at room temperature, where this crystal orientation is typically randomly distributed.[14]

It has been reported that, especially in the case of steel, the slip plane becomes separated to form QCF,[8] and it has been further reported that such QCF is not of the slip-plane variety.[7,15] In order for the slip plane to separate, it is

necessary to trap a huge amount of hydrogen along this locations that mobile on slip planes. On the other hand, quasi-cleavage planes have been observed in the case of hydrogen embrittlement in aluminum and some new reports are available recently. Yamaguchi *et al.* investigated the hydrogen trap energies for vacancies, dislocations, grain boundaries, pores/nanovoids, precipitates, and intermetallic compounds, in aluminum.[16–20] They found that the hydrogen trap energies for edge dislocation and screw dislocation were 0.15 eV and 0.08 eV, respectively, both of which were as low as expected.[16] Grain boundary has also been reported as a weak hydrogen trap site, with a hydrogen trap energy of 0.25 eV found in one study.[17] Others studies have found that the hydrogen trap energy for $MgZn_2$ precipitates ($\eta$ phase) was 0.35 eV at the coherent precipitate/matrix interface[18] and 0.56 eV at the semi-coherent interface.[19] The energy inside an $Al_7Cu_2Fe$ intermetallic compound was 0.56 eV,[20] that of absorption atomic hydrogen to pore surface was

0.67 eV, and that of molecular hydrogen inside the pore was 0.70 eV.[21] Experiments involving X-ray nanotomography and X-ray microtomography and TEM observation have precisely measured the trap site densities of these hydrogen trap site.[22–24] Using the microstructure tracking technique, the trap site densities of geometrically necessary dislocations (GNDs), statistically stored dislocations (SSDs), and vacancies have been measured at a spatial resolution of 1 μm by mapping the 3D plastic strain inside materials.[22,23] In addition, these trap site densities have been measured even during deformation, which enabled measurement of the dynamic trap site density change at the tip of propagating cracks.[19] These results show that the coherent and semi-coherent interfaces of precipitates, which have a remarkably high trap site density, act as high hydrogen trap energy sites for 90% of the total hydrogen in the material; and further, that the hydrogen occupancy at these trap sites is extremely high. According to this analysis, the hydrogen occupancy at dislocation and grain boundary trap sites is in the order of $10^{-7}$ and $10^{-8}$.[19] It is unreasonable to assume that precipitate/matrix interfaces and grain boundaries are debonded at such low hydrogen concentrations. The results of the study clearly negate the conventional hypothesis that QCF originates from slip-plane decohesion. On the other hand, Tsuru *et al.* have reported interesting results of first-principles calculations, which show that the phase boundaries and coherent interfaces of precipitates are semi-spontaneously debonded when many hydrogen atoms are present on those planes, even without the application of external loads.[24] According to that study, interfacial debonding starts at 18.9 atomH/nm$^2$, which is roughly two orders of magnitude greater than the hydrogen concentration in precipitates surface (0.1 atomH/nm$^2$) as reported by Shimizu.[23] Complete interfacial debonding occurs at 37.7 atomH/nm$^2$, where the hydrogen becomes molecular to intervene between separated interfaces. High precipitate densities have, in fact, been observed on QCF surfaces, which supports the results of first-principles calculations.[24] Precipitates are several 10 nm in diameter, and it might be difficult to measure their crystallographic orientations on fracture surface using conventional methods. However, it is expected that the predicted phenomena will eventually receive experimental confirmation. Precipitates have a specific crystallographic orientation, with the matrix ([0001]MgZn$_2$//[111]Al),[25] and it is reasonable to assume that the fracture surface will be characterized by specific crystallographic planes when the precipitate/matrix interfaces have been debonded. However, unlike in steels, in aluminum alloys, the surface energy does not differ significantly among different crystallographic planes. For example, the (111) plane has the lower surface energy, at 0.531 eV/atom, while the (110) plane has the higher surface energy, at 0.919 eV/atom; a much smaller ratio than in the case of steels, which exhibit a ratio of 2.8 between the (110) and (111) plane[26]. Consequently, although the crystallographic plane for (local) interfacial debonding of the precipitate/matrix interface is well defined, the overall fracture surface may deviate from this plane. Precipitates satisfying interfacial debonding criteria such as hydrogen concentration will nucleate diffuse, local damage with sub-micrometer sized crystallographic facets but the overall fracture surface is formed by microcrack coalescence. Its local orientation will depend on the spatial distribution and arrangement of the nucleation sites, resulting in a fracture surface which is almost independent of crystallographic plane as has been clarified in the present study.

## 4. Conclusions

Crystallographic assessment of the hydrogen embrittlement behavior in aluminum alloy was performed by combining fracture trajectory analysis and diffraction contrast tomography. The fracture surface consisted of IGF, DF, and QCF surfaces. The IGF crack initiated at a grain boundary with high grain boundary energy and a high angle between the grain boundary plane and loading direction; however, the crack propagated without dependence on the grain boundary energy or the angle between the grain boundary planes. In the case of QCF, the QCF surface was not characterized by any specific crystal orientation.

## REFERENCES

1) L. Christodoulou and H.M. Flower: Acta Metall. **28** (1980) 481–487.
2) D. Nguyen, A.W. Thompson and I.M. Bernstein: Acta Metall. **35** (1987) 2417–2425.
3) N. Takano: Mater. Sci. Eng. A **483–484** (2008) 336–339.
4) G.M. Bond, I.M. Robertson and H.K. Birnbaum: Acta Metall. **35** (1987) 2289–2296.
5) M.S. Bhuiyan, Y. Tada, H. Toda, S. Hang, K. Uesugi, A. Takeuchi, N. Sakaguchi and Y. Watanabe: Int. J. Fract. **200** (2016) 13–29.
6) N. Takano, K. Kidani, Y. Hattori and F. Terasaki: Scr. Metall. Mater. **29** (1993) 75–80.
7) A. Nagao, C.D. Smith, M. Dadfarnia, P. Sofronis and I.M. Robertson: Acta Mater. **60** (2012) 5182–5189.
8) K. Okada, A. Shibata, Y. Takeda and N. Tsuji: Int. J. Hydrogen Energy **43** (2018) 11298–11306.
9) H. Toda, H. Oogo, K. Horikawa, K. Uesugi, A. Takeuchi, Y. Suzuki, M. Nakazawa, Y. Aoki and M. Kobayashi: Metall. Mater. Trans. A **45** (2014) 765–776.
10) W. Ludwig, P. Reischig, A. King, M. Herbig, E.M. Lauridsen, G. Johnson, T.J. Marrow and J.Y. Buffiere: Rev. Sci. Instrum. **80** (2009) 033905.
11) W.E. Lorensen and H.E. Cline: SIGGRAPH '87 Proceedings of the 14th Annual Conference on Computer Graphics and Interactive Techniques, (ACM, New York, NY, USA, 1987).
12) W.T. Read and W. Shockley: Phys. Rev. **78** (1950) 275–289.
13) D. Wolf: Scr. Metall. **23** (1989) 1712–1718.
14) J.D. Defilippi: Trans. Met. Soc. AIME **245** (1969) 2141.
15) Y.H. Kim and J.W. Morris, Jr.: Metall. Trans. A **14A** (1983) 1833–1888.
16) M. Yamaguchi, M. Itakura, T. Tsuru and K. Ebihara: Mater. Trans. **62** (2021) 582–589.
17) M. Yamaguchi, K. Ebihara, M. Itakura, T. Tsuru, K. Matsuda and H.

Toda: Comput. Mater. Sci. **156** (2019) 368–375.

18) T. Tsuru, M. Yamaguchi, K. Ebihara, M. Itakura, Y. Shiihara, K. Matsuda and H. Toda: Comput. Mater. Sci. **148** (2018) 301–306.

19) K. Shimizu, H. Toda, K. Hirayama, H. Fujihara, T. Tsuru, M. Masatake, A. Bendo, K. Matsuda and A. Takeuchi: [unpublished work].

20) M. Yamaguchi, T. Tsuru, K. Ebihara, M. Itakura, K. Matsuda, K. Shimizu and H. Toda: Mater. Trans. **61** (2020) 1907–1911.

21) M. Yamaguchi, T. Tsuru, K. Ebihara and M. Itakura: J. JILM **68** (2018) 588–595.

22) H. Su, H. Toda, K. Shimizu, K. Uesugi, A. Takeuchi and Y. Watanabe: Acta Mater. **176** (2019) 96–108.

23) K. Shimizu, H. Toda, H. Fujihara, K. Hirayam, K. Uesugi and A. Takeuchi: Eng. Fract. Mech. **216** (2019) 106503.

24) T. Tsuru, K. Shimizu, M. Yamaguchi, M. Itakura, K. Ebihara, A. Bendo, K. Matsuda and H. Toda: Sci. Rep. **10** (2020) 1998.

25) J. Gjønnes and C.J. Simensen: Acta Metall. **18** (1970) 881–890.

26) L. Vitos, A.V. Ruban, H.L. Skriver and J. Kollár: Surf. Sci. **411** (1998) 186–202.